Growth of Turbulent Boundary Layer with Varying Inlet Length Scales

Y. T. Lee and H. C. Lim[†]

School of Mechanical Engineering, Pusan National University, 2, Busandaehak-ro 63beon-gil, Geumjeong-gu, Busan,46241, Republic of Korea

†*Corresponding Author Email: hclim@pusan.ac.kr*

ABSTRACT

This study aims to generate a fully developed turbulent boundary layer in the channel domain using LES (Large Eddy Simulation), suitable inflow conditions along with statistically reliable turbulent characteristics are required. This study clarifies the effect of the integral length scale from the existing data on the generation of turbulent boundary layers. In order to justify the work, an artificially created boundary layer is imposed on the inlet section, which gradually evolves into a fully developed turbulent boundary layer flow inside the numerical domain. In this study, the synthetic inflow method, which is based on an exponential correlation function, is used by imposing the spatial and temporal correlation between two different points on the inlet section. In addition, we conducted parametric length scale studies on the inlet section and compare our results with existing data. The results indicated that the cases of larger length scale in the span-wise direction were not only effective in achieving the target shape of a fully developed turbulent boundary layer, but also developed it faster than the smaller-length scales.

Keywords: Statistical inflow data; Synthetic inflow generator; Integral length scale; Channel flow; Turbulent boundary layer; CFD.

NOMENCLATURE

$a_{ij}\psi_j$	fluctuating part of u_i	u_i	instantaneous velocity
b_j	filter coefficient	$\overline{u_i}$	mean part of u_i
C_s	Smagorinsky constant	$\overline{S_{ij}}$	filtered rate of strain tensor
d	half height of the channel	t_*	non-dimensional time
L	integral length scale	u_τ	friction velocity
r_m	random number	Δx	grid size
Re_{ij}	Reynolds stress	δ_{ij}	filtered static pressure
Re_τ	Reynolds number	ψ_j	amplitude tensor
T	Eulerian time scale	ϕ_m	velocity field

1. INTRODUCTION

The most direct method of generating a well-developed turbulent boundary layer is to simulate a laminar inflow and allow it to develop spatially over a suitably long domain, i.e. over a hundred times the thickness of the eventual boundary layer depth of interest. However, even this 'simple' method would present difficulties associated with ensuring the correct surface conditions, such as the length scale and wall treatment. Further, the computational cost would be very high. Alternatively, using a time-evolving large-eddy simulation (LES) or direct numerical simulation (DNS) with a periodic (Lee *et al.* 1992, Keating *et al.* 2004, Lim *et al.* 2009) or a 'modified periodic' (Lund *et al.* 1998), the inlet-outlet boundary condition can be used to generate the appropriate turbulent flow. For the latter, one of the authors used a sort of 'precursor simulation', in which the velocity field at an appropriate downstream station is stored and imposed in a suitably re-scaled form as the inflow data for the

primary computation. (Lim *et al.* 2009) The precursor simulation generates a realistic turbulent flow field. However, it is also expensive and has limitations, such as its applicability to simple geometries only. Therefore, it is difficult to determine the usefulness of such a method in actual urban-type scenarios.

Procedures which are based on proper orthogonal decomposition (Druault *et al.* 2004, Johansson and Andersson 2004, Perret *et al.* 2006)may be less expensive than the above methods for the generation of inflow data provided that there are appropriate DNS/LES (Johansson and Andersson 2004)or experimental datasets (Druault *et al.* 2004, Perret *et al.* 2006)available for processing in order to obtain the most energetic modes, with an appropriate set of time-dependent projection coefficients that provide the phase information. The reconstructed inflow data for later LES/DNS are 'almost statistically realistic'. However, the experimental databases suffer from either low spatial resolution, which is common in measurements from hot-wire or laser Doppler anemometry (Druault *et al.* 2004), or low temporal resolution, as obtained from measurements using particle-image velocimetry (Perret *et al.* 2006).

Special treatment must then be applied to resolve the issues pertaining to its low resolution. Consequently, such approaches are generally suitable only for very specific cases; synthetic turbulence generation is another option, and is of particular interest when only limited turbulence statistics data are available. Hanna *et al.* (2002) generated one-dimensional (1D) time series of inflow data based on an exponential correlation function to simulate flows over an array of cubes using LES. The time series were tailored to provide the required time scale and turbulence intensities, and the subsequent LES was able to reproduce the main characteristics of the measurements. The merit of that method is its very high efficiency; however, its accuracy is seriously limited because no spatial correlation was imposed at the inlet.

Because of the features of the atmospheric boundary layer flows as an inflow condition, one of the representative studies would be the work of Xie and Castro (2008). They used the urban boundary layer flows, which should have a high Reynolds number, and fully developed turbulence driven by large-scale motions. They used a digital filter-based method, which allows spatially varying turbulence scales on non-uniform grids to be imposed at the inlet. It was developed independent of the works of Mare *et al.* (2006), Veloudis *et al.* (2007), whose methods are similar in some respects, and have already been used elsewhere (Jarrin *et al.* 2006).

Therefore, this study investigated the flow characteristics in a channel with a smooth wall by imposing synthetic inflow data having a statistically varying length scale. Various inflow length scales were imposed to examine their effect on the whole flow domain with the aim of observing the relationship between the length scale and the development of the turbulent boundary layer. This paper is organised as follows: In Section 2, the

governing equation and synthetic inflow generation using the digital filtering method for the LES inlet condition are introduced and summarised. This is confirmed by making a comparison with the turbulent statistics from an existing DNS database. In Section 3, the synthetic inflow generation technique was validated by the simulation of a smooth wall-bounded channel flow. Furthermore, the characteristics of the turbulent boundary layers simulated by LES using inlet data imposed by the synthetic inflow generation are analysed. In addition, the effects of the inlet length scales on the development of a flow structure inside the flow domain are also investigated. Finally, Section 4 concludes this study.

2. NUMERICAL ANALYSIS

2.1 Governing equation

To resolve the incompressible flow, we must estimate the flow structure for a wide range of scales. The DNS method can resolve a wide range of scales, from large ones to the Komogorov, which is the smallest scale. However, until now, its computational cost has been too high for it to be used as a design tool. LESs can adequately substitute the DNS method in simulating turbulent flow. Furthermore, it has a substantially reduced computation cost, and has become one of the main methods for investigating complex turbulent flows with a relatively high Reynolds number. LESs resolve only a large scale of motion, and the effect of smaller scales is modelled by the sub-grid scale (SGS) modelling. The LES scheme has had a considerable influence on the development of turbulent flows.

In LESs, the governing equations for a large eddy are applied after a spatial filtering operation. The spatial filtering operation is given by

$$\bar{f}(x) = \int G(x-x')f(x')dx' \tag{1}$$

where f is a turbulent field and G is a spatial filter.

The continuity and momentum equation for incompressible flows are obtained by filtering the Navier–Stokes equations. The filtered Navier–Stokes equations are given by

$$\frac{\partial \bar{u}_i}{\partial x_i} = 0 \tag{2}$$

$$\frac{\partial \bar{u}_i}{\partial t} + \bar{u}_j \frac{\partial \bar{u}_i}{\partial x_j} = -\frac{1}{\rho}\frac{\partial \bar{p}}{\partial x_i} + 2\nu \frac{\partial}{\partial x_j}\bar{S}_{ij} - \frac{\partial \tau_{ij}^r}{\partial x_j} \tag{3}$$

where τ_{ij}^r is the residual stress tensor. τ_{ij}^r is given by

$$\tau_{ij}^r = \overline{u_i u_j} - \bar{u}_i \bar{u}_j \tag{4}$$

In Eq.(4), the residual stress tensor is unknown and should be modelled.

The eddy viscosity Boussinesq hypothesis is used for modelling the residual stress tensor as follows:

$$\tau_{ij}^{r} = -2\mu_t \bar{S}_{ij} + \frac{1}{3}\tau_{kk}\delta_{ij} \tag{5}$$

where μ_t is the turbulent viscosity of the sub-grid scale. The isotropic part of δ_{ij} is added to the filtered static pressure term without being modelled. In Eq.(5), $\bar{S}_{ij}$ is the filtered rate of strain tensor and is defined by

$$\bar{S}_{ij} = \frac{1}{2}\left(\frac{\partial \bar{u}_i}{\partial x_j} + \frac{\partial \bar{u}_j}{\partial x_i}\right) \tag{6}$$

The Smagorinsky-Lilly model was used as a subgrid-scale model. In this study, the Smagorinsky constant C_s, was set to 0.065 (Moin and Kim 1982).

2.2 Modelling of inflow generator

We investigate a synthetic inflow generator having a variety of length scales, which is based on Xie and Castro's method (Xie and Castro 2008). In this section, we present a brief review of their model, which imposes correlations using an exponential function to satisfy the prescribed space and time correlations. The instantaneous value of the velocity u_i may be written as

$$u_i = \bar{u}_i + a_{ij}\psi_j \tag{7}$$

where $\bar{u}_i$ is the mean, and $a_{ij}\psi_j$ is the fluctuating part of u_i, which is called Reynolds decomposition. The fluctuating part can be separated into two parts, a_{ij}, which is the amplitude tensor, and ψ_j, which is the unscaled fluctuation with zero mean ($\bar{\psi}_j = 0$), a unit variance ($\overline{\psi_j\psi_j} = 1$), and zero covariance with the other distributions ($\overline{\psi_j\psi_j} = 0, i \neq j$). The term a_{ij} using Reynolds stress R_{ij} is the Cholesky decomposition of the Reynolds stress by Le and Moin (2005) as follows,

$$a_{ij} =$$
$$\begin{pmatrix} \sqrt{R_{11}} & 0 & 0 \\ R_{21} & \sqrt{R_{22} - a_{21}^2} & 0 \\ R_{31}/a_{11} & (R_{32} - a_{21}a_{31}/a_{22}) & \sqrt{R_{33} - a_{31}^2 - a_{32}^2} \end{pmatrix} \tag{8}$$

where R_{ij} is the Reynolds stress tensor obtained from the experimental or previously calculated numerical simulation data. If the boundary layer is homogeneous in the lateral direction, $R_{31} = R_{32} = 0$; therefore, a_{31} and a_{32} can be removed.

The synthetic inflow generation technique using digital filtering aims to find the unscaled fluctuation (ψ_j), which is a 1-dimensional number sequence with zero mean, unit variance, and spatial correlation. The correlations in the most turbulent shear flow have similar features. The advantage of the correlation function is that it approximates the relation of two different points to the form of an exponential function. The exponential function is $\exp(-\pi r / \beta L)$, where β is a constant. However, in the quation, β is not clearly defined, and its function remains unclear. In this study, the exponential function was carefully tested and subsequently modified. Kim *et al.* 2013 used the modified exponential function as follows (Kim *et al.* 2013):

$$R(r,0,0) = exp(-\frac{\pi r}{4L}) \tag{9}$$

where L is the integral length scale. The filter is designed to process a series of random numbers using an exponential function. Taking a filter coefficient and a series of random numbers into account, the velocity field is derived as follows:

$$\psi_m = \sum_{j=-N}^{N} b_j r_{m+j} \tag{10}$$

where ψ_m, b_j, and r_m are the velocity field, filter coefficient, and a series of random numbers with zero mean ($\bar{r}_m = 0$), respectively, and unit variance ($\overline{r_m r_m} = 1$). In addition, the integral length scale (L) can be considered as a multiple of the grid size (Δx) and expressed as $L = n\Delta x$. In addition, N is determined by the integral length scale. The relation between N and n was also carefully tested for $N \geq 2n$, and finally, $N = 2n$ was accepted. In this study, the variation of the length scale was made in the inlet section. Using Eqs. (9) and (10), the filter coefficient b_j could be defined as shown in Eq.(11).

$$b_j = (\tilde{b}_j)/\left(\sum_{k=-N}^{N} \tilde{b}_k^2\right)^{1/2}, \quad \tilde{b}_j = exp\left(-\frac{\pi|j|}{2n}\right) \tag{11}$$

Based on these equations, 1D data satisfying the required length scale L, mean $\bar{\psi}_m = 0$, and variance $\overline{\psi_m\psi_m} = 1$ can be obtained. The filter coefficient for a two-dimensional (2D) plane can be obtained by the convolution of two 1D filter coefficients, $b_{jk} = b_j b_k$. It is expressed as follows:

$$\psi_{m,l} = \sum_{j=-N}^{N} \sum_{k=-N}^{N} b_{jk} r_{m+j,l+k} \tag{12}$$

In the first time step, the velocity data of a plane are generated by applying the filter to the random number on the 2D plane. The data $\psi_j(t,y,z)$ of the 2D plane is set to have a constant length scale, $L_i = n_i\Delta tx_i$, in the vertical direction and in the span-wise direction. To impose a more precise length scale, it is also possible to divide the region of the
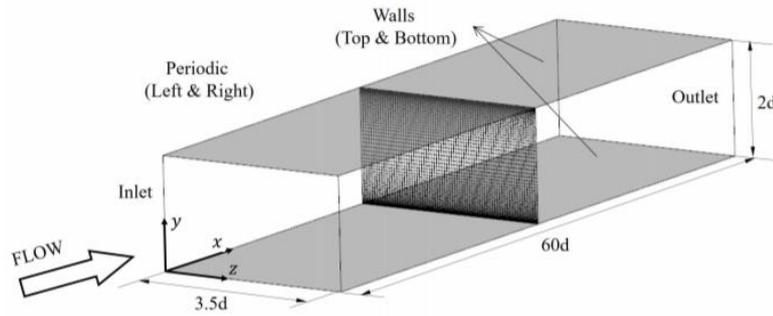
Fig. 1. Schematic diagram of computational domain. (total number of cells: $600 \times 60 \times 70$).

inlet plane and apply different length scales at each region. The time scale should be considered for application of the plane velocity field data for the next time step. Based on Taylor's hypothesis, the Lagrangian time scale can be expressed as follows:

$$T = L / \bar{u} \tag{13}$$

where L is the length scale and $\bar{u}$ is the local mean velocity. In addition, the Eulerian time scale, T, can be obtained from experimental or previous numerical analyses. The velocity of the next time step can be calculated by Eq. (14) using the velocity at the previous time step.

$$\psi_i(t+\Delta t, y, z) = \psi_i(t, y, z)\exp\left(-\frac{\pi\Delta t}{4T}\right)$$
$$+ \psi_i(t, y, z)\left[1 - exp\left(-\frac{\pi\Delta t}{2T}\right)\right]^{0.5} \tag{14}$$

where ψ_i is obtained using a new set of random data; however, ψ_i is the plane velocity field data of the current or next time step and T is a constant value for the entire inlet plane representing the Eulerian time scale. Note that ψ_i is fully random in time, its variance is unity, and it is an independent variable from $\psi_i(t, y, z)$.

2.3 Implementation of boundary condition and inflow length scale

In this study, a hexahedral grid system was used for the numerical simulation of an efficient turbulent flow. To improve the convergence efficiency in the solution of the governing equations, a stretched mesh was used so that the grid was concentrated on the wall surface and the resolution was sufficiently high close to the wall, but coarse at the far field from the wall. The Reynolds number (Re_τ) on the smooth wall-bounded channel flow was 150 based on the friction velocity (u_τ) and the half height (d) of the channel. The size of the whole computational domain was $60d \times 2d \times 3.5d$ in the streamwise (x), wall normal (y), and spanwise (z) directions, respectively. The number of cells in the whole domain was approximately 2.5 million, as shown in Fig.1. To improve the convergence of the analysis, a stretched mesh satisfying $y^+ < 1$ in the first cell center was considered for the wall-normal direction. For the x and z directions, uniform meshes were used and the resolutions were $\Delta x^+ = 15, \Delta z^+ = 7.5$. The number of cells in each direction was $600 \times 60 \times 70$ in the x, y, and z directions, respectively. All statistics were averaged by $40t_*$, where $t_* = tu_\tau / d$ is a non-dimensional time. Averaging for the statistical analysis was performed after the initialisation period of $20t_*$. The Smagorinsky subgrid-scale model was adopted with a constant $c_s = 0.065$ (Iwamoto *et al.* 2002). The time step satisfies the condition that the CFL number should be smaller than 1. The corresponding $\Delta t_* = \Delta t \times u_\tau / \delta = 0.001$. A second order implicit scheme was used for time discretization, and a second order central difference scheme was used for spatial discretization. Furthermore, the transient incompressible flow solver was used, and the PISO algorithm was adopted as the velocity-pressure coupling scheme. In addition, the PRESTO algorithm was used as a discretization technique for pressure.

The boundary conditions of this channel flow are: no-slip condition on the top and bottom walls, periodic boundary condition in the lateral direction, and a zero-gradient condition with no diffusion of all the flow variables on the outlet. The synthetic turbulence obtained by the synthetic inflow generator was interpolated into the cell centre of the inlet plane. The turbulence information, including the first and second moment statistics and the integral length scales used as input parameters to generate the synthetic inflow, were obtained from the DNS database that analysed the plane channel flow (Iwamoto *et al.* 2002). The integral length scale L_i is obtained using Eq.15 with a two-point correlation and $R(x_i)$ in the DNS database.

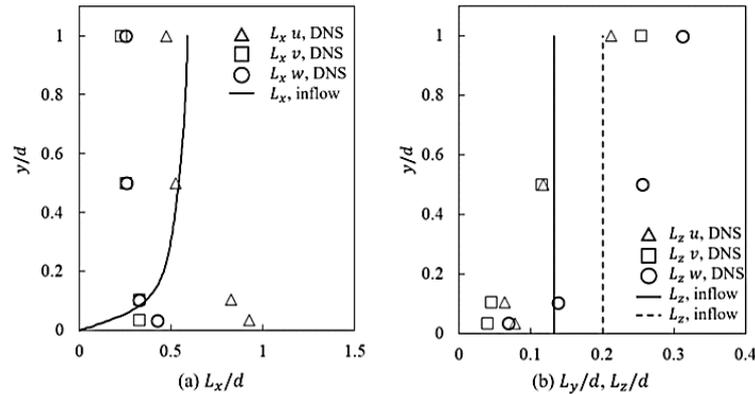$$L_i = \int_0^\infty R(x_i)dx_i, \ i = 1, 2, 3 \tag{15}$$

Fig. 2. Integral length scales (symbol: two-point correlation in DNS data; line: inflow generation).

Figure 2 shows the length scale obtained from the DNS database and the simplified length scale applied to the synthetic inflow generation. Figure 2(a) shows the distribution of the streamwise direction length scale, L_x, along the wall-normal direction.

If the relative turbulence intensities are sufficiently low, according to Taylor's hypothesis, the length scale can be determined by the local mean velocity $\bar{u}$ and the Eulerian time scale T. Therefore, $L_x(y) = T \times \bar{u}(y)$ is applicable (Taylor 1938). In the equation, T is a constant, and the local mean velocity in the stream-wise direction increases with the distance from the wall, and the stream-wise length scale also becomes large. In this study, the turbulence intensity of the flow simulation is smaller than 0.3, and Taylor's hypothesis can therefore be applied across the entire domain. However, the stream-wise length scale obtained from the actual DNS is highest close to the wall and gradually decreases in the freestream. To impose a precise stream-wise length scale of actual DNS data as the inlet condition, the three-dimensional (3D) domain should be considered when generating the fluctuating part, ψ_i. The advantage of the inflow generation technique considered in this study is that it can generate efficient inlet velocity field data at every time step only on the 2D plane, while matching the second-order turbulent statistics obtained from the experiment or a previously calculated simulation. Figure 2(b) shows the length scale for the y and z directions. Notably, there are no DNS data of a length scale in the wall-normal direction (y) in the existing literature. Therefore, because it is in-homogeneous for the wall-normal direction, we assumed in the study that $L_y = 0.67 L_z$ for the length scale in the y direction. (see Iwamoto *et al* 2002) As mentioned above, the entrance plane can be divided into several sections, and different values of L_y and L_z have been applied to each section.

2.4 Variation of inflow length scale

In this study, the flow characteristics were observed with variations in the integral length scales at the inlet section. As mentioned earlier, the stream-wise local length scale, $L_x(y)$, is determined by the local mean velocity, $\bar{u}(y)$, and the constant time scale, T, where the constant T could be obtained by L_x and $\bar{u}$ at $y/d = 1$. The span-wise length scale could be applied as a multiple of L_z^*, where L_z^* is the reference span-wise length scale, which is equivalent to the value L_z used in Fig. 2. To observe the effect of the L_z distribution on the flow field, this study chose several different values, such as $0L_z^*$ (white noise), $0.15L_z^*$, $0.3L_z^*$, $0.5L_z^*$, $2L_z^*$, $3L_z^*$ (see Table 1). To achieve a precise matching with the L_z^* distribution of the existing DNS database, in the length scales L_z^* the domain needed to be divided into three different zones. These zones were separated in several salient positions at $y/d = 0.1, 0.2$. Table 1 presents the configuration of each case depending on the size of the length scale in each zone. For instance, Case 02 does not consider the length scale in the inlet condition, whereas Cases 01, 07, and 08 have a uniform span-wise length scale in L_z. Besides, to observe the effect of different length scales on different zones, Cases 03, 04, 05, and 06 would play an important role, in addition to studying the variation of flow statistics based on length scales. In particular, Cases 07 and 08 have length scales that are two and three times larger, respectively, than that of Case 01 for all the stream-wise, vertical, and span-wise directions.

2.5 Filtering process and correlation

This study adopted the filtering process in which random data are filtered and correlated to obtain fluctuating data in ψ_m. When the series of random numbers is filtered through the synthetic inflow model used in this study, the filtered velocity field data, which are similar to the fluctuating part of the flow, are obtained. To apply this algorithm to the synthetic inflow generator, the velocity field data are first generated in a 2D equi-spaced uniform mesh, and then interpolated into a non-uniform mesh with

Table 1 Size of length scales applied in the simulation.

Name	$y/d<0.1$	$0.1<y/d<0.2$	$y/d>0.2$
Case 01	$1Lz*$	$1Lz*$	$1Lz*$
Case 02	0, random	0, random	0, random
Case 03	$0.15Lz*$	$0.15Lz*$	$0.5Lz*$
Case 04	$0.3Lz*$	$0.3Lz*$	$1Lz*$
Case 05	$0.5Lz*$	$0.5Lz*$	$1.5Lz*$
Case 06	$0.3Lz*$	$1Lz*$	$1Lz*$
Case 07	$2Lz*$	$2Lz*$	$2Lz*$
Case 08	$3Lz*$	$3Lz*$	$3Lz*$
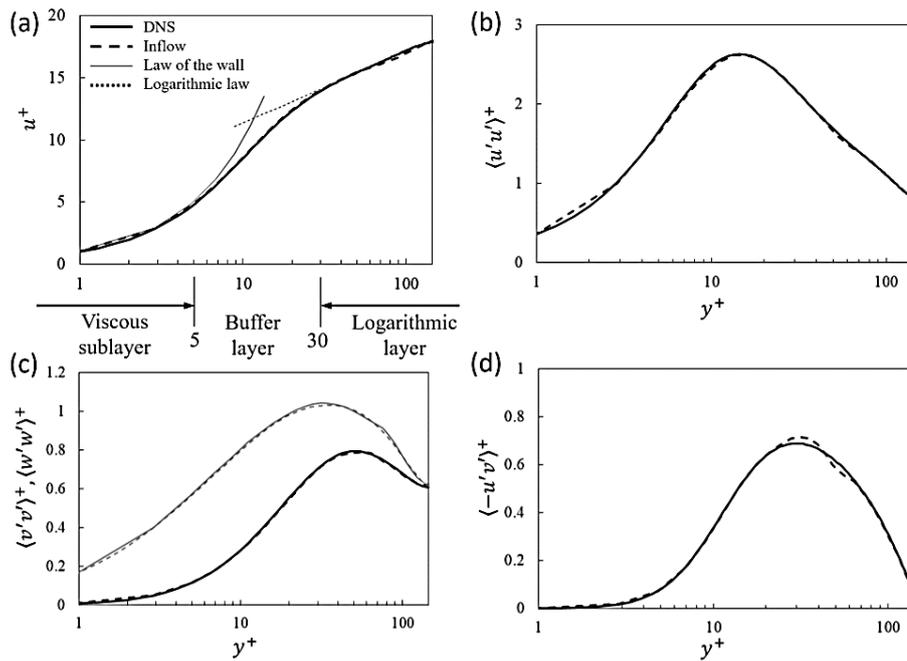
Fig. 3. Statistical profiles from DNS and synthetic inflow generator.

the aim of fitting it into the more realistic inlet domain as an inlet condition.

Figure 3 compares the DNS database with the data from the synthetic inflow generator for the mean and turbulent statistics. The non-dimensional parameters used here can be defined as follows:

$$y^+ = \frac{u_\tau y}{\nu}, \, u^+ = \frac{u}{u_\tau}, \, \langle u'v'\rangle^+ = \frac{\langle u'v'\rangle}{u_\tau^2} \qquad (16)$$

In the figure, the ordinate axis shows the non-dimensional mean and stress profiles, and the abscissa represents the non-dimensional distance from the wall (y^+). In the mean velocity profile u^+ , the current result agrees well with the overall range of the domain, such as the law of the wall at $y^+<5$ and the logarithmic law at $y^+>30$. In addition, it can be seen that the axial and shear stresses from the synthetic inflow generator are in good agreement with the DNS data.

3. RESULTS AND DISCUSSION

3.1 Channel flow simulation using synthetic inflow generator

Given that the synthetic inflow generator was available, the channel flow simulation on the LES platform was initially conducted with the aim of observing the development of the turbulent flow in the whole domain. The channel flow starts with the data from the synthetic inflow generator, adopting it in the inlet section, and develops the flow downstream to the smooth wall-bounded channel. The development of axial and shear stress profiles are very important for identifying the fully developed flow, (Kim *et al.* 2013, Deck *et al.* 2011)as well as obtaining an appropriate turbulent flow downstream.

Figure 4 shows the development of dimensionless axial and shear stress distributions. Figure 4(a) indicates the variation in the wall shear stress close to the surface from the inlet to downstream of the
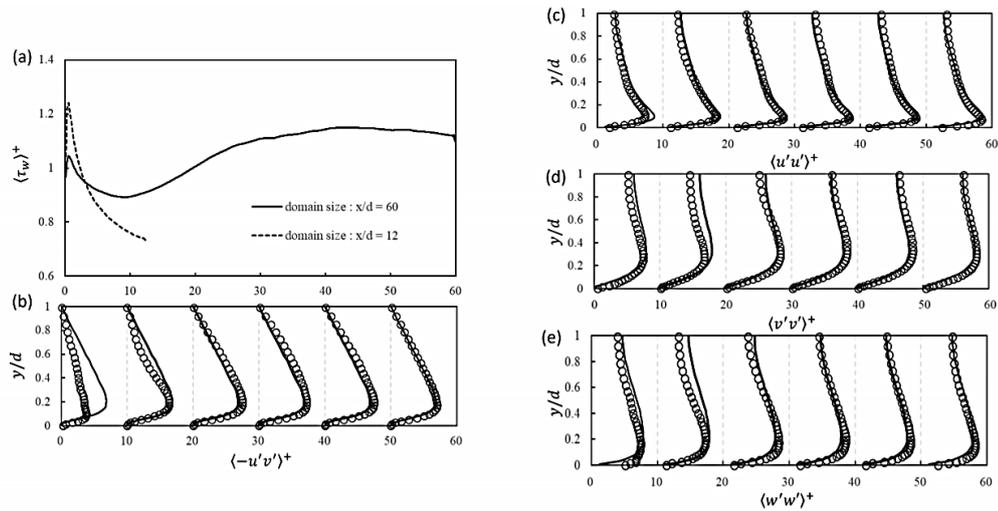
Fig. 4. Spatial development of (a) dimensionless wall shear stress, (b) shear stress, (c) axial stress (longitudinal), (d) axial stress (vertical), (e) axial stress (spanwise).

channel; the ordinate axis indicates the non-dimensional wall shear stress, defined as $\langle\tau_w\rangle^+ = \tau_w / (\rho u_\tau^2)$, and the abscissa represents the stream-wise distance (x) from the inlet normalised by the half height (d) of the channel. To observe the effect of the longitudinal domain size, two different domains ($x / d = 12$ and 60) were designed and calculated. As shown in the figure, the wall shear stress decreases near the inlet of the channel and slowly recovers downstream, becoming almost constant at around $x / d = 30$ (see solid line). Moreover, the short domain case $(x / d = 12)$ did not recover (see dashed line), and the difference between the highest and lowest magnitudes of $\langle\tau_w\rangle^+$ was much larger than that of the domain size $x / d = 60$. Therefore, if the domain size is set to be less than $x / d = 30$, the wall shear stresses would be very low. Figure 4(b) shows the Reynolds stress profiles at several equi-spaced positions, x/d = 0, 10, 20, 30, 40, and 50, and the abscissa indicates the wall-normal distance from the wall surface normalised by d.

Figure 4(c-e) indicates the variation of axial stress profiles along the whole domain. Note here that the solid lines in the figure represent the existing DNS data. The axial (longitudinal) stress profiles begin initially with the data from the synthetic inflow generator; however, they gradually develop and reach the fully developed profile downstream, which corresponds to the existing DNS data. The vertical and span-wise stress profiles were also not properly developed upstream, but they had almost fully developed downstream.

Figure 5 shows the gradient of the dimensionless shear stress, $\langle\tau_w\rangle^+ / \Delta x$, in the stream-wise direction with the aim of identifying more precisely the critical point indicating a fully developed boundary layer. As shown in Fig.5 , there is a steep gradient near the

inlet, and the values $\langle\tau_w\rangle^+ / \Delta x$ gradually recover and converge to an almost constant value (i.e. around zero) in the region where $x / d \geq 40$.
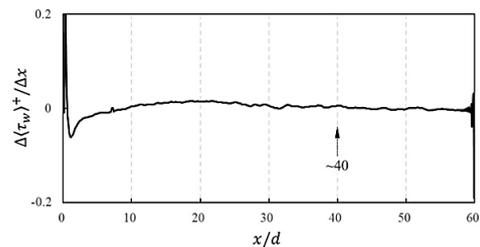

Fig. 5. Variation of dimensionless wall shear stress per grid size.

Figure 6 shows the mean and turbulent statistics in the channel flow, and compares them with the existing DNS data (Kim *et al.* 1987). In the figure, the fully developed profile was obtained at x/d = 50, and the inlet data from the inflow generator and the DNS results for the reference and existing data were also compared. As shown in the figure, most of the profiles agree perfectly well with each other, which is very satisfactory. The turbulent statistics for both cases, that is, the inlet and x/d = 50, also show a similar pattern. In particular, the non-dimensional mean velocity, u^+, is almost identical. The axial longitudinal stress profile, $\langle u'u'\rangle^+$ at x/d = 50 also shows a similar distribution near the wall surface compared to that at the inlet. However, when y/d is between 0.1 and 0.4, it is relatively lower than that at the inlet, whereas it is relatively high for y/d between 0.4 and 1.0. The axial vertical stress profile, $\langle v'v'\rangle^+$, and the shear stress, $\langle -u'v'\rangle^+$, at x/d = 50 were
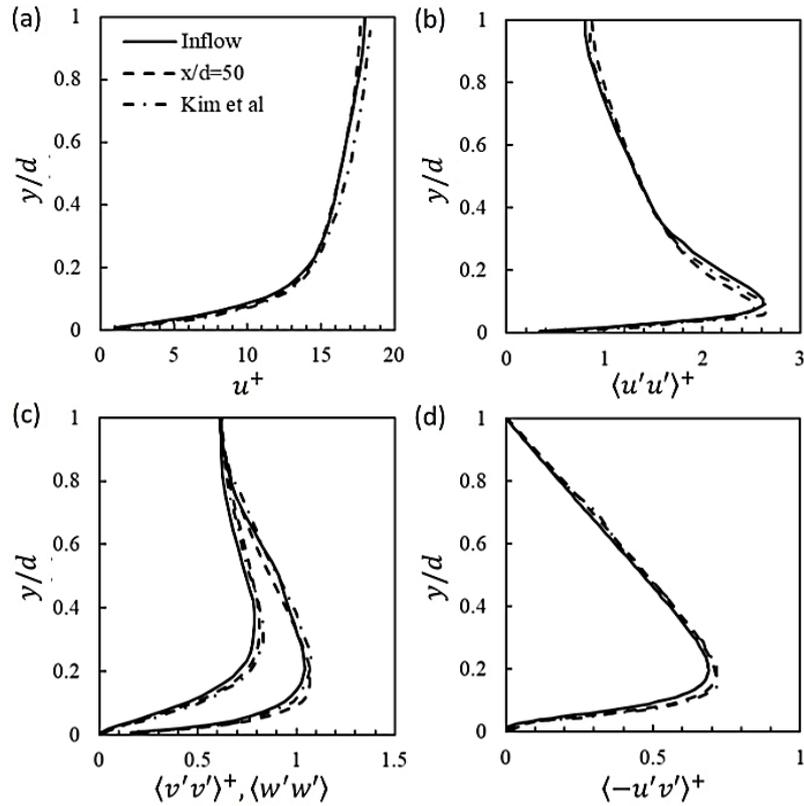
Fig. 6. Mean and turbulent statistics in channel flow at the inlet, x=d = 50, in an existing study.
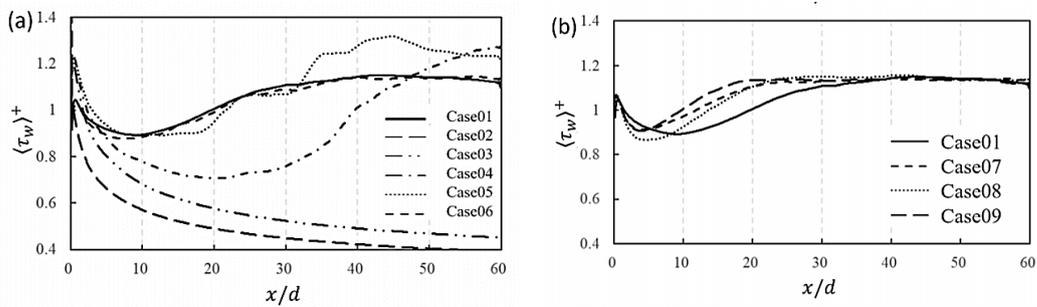(**Kim** *et al.* **1987**)

Fig. 7. Development of dimensionless wall shear stress with different length scales.

slightly overestimated compared to the data at the inlet. The difference between the turbulent boundary layers at the inlet and x/d = 50 is due to a relatively coarse resolution of the LES in the core region.

3.2 Effect of inlet length scale on wall shear stress

Figure 7 shows the distribution of the non-dimensional wall shear stress $\langle \tau_w \rangle^+$ for all the cases of different inlet length scales. Notably, the stream-wise length scales are the same for all those cases. To observe the effect of the length scale close to the wall, the span-wise length scale was set from a minimum of $0.15 L_z^*$ to a maximum of $3 L_z^*$. It

should be noted that the variation in the inlet length scale has a significant effect on the recovery of the wall shear stress downstream. As shown in Fig.7(a), Case 01 reveals that the wall shear stress recovered fairly well at x/d = 40. The wall shear in other cases having a relatively smaller length scale than that in Case 01 is mostly unstable and does not properly recover downstream, except in Case 06.

In Case 02, which is the worst case having no length scale implemented in the inflow, the wall shear stress continuously decreases downstream, and the wall shear stress substantially drops to approximately 50 \% at the outlet compared to that at the inlet. Case 03, in which the length scale is $0.15 L_z^*$, is used in
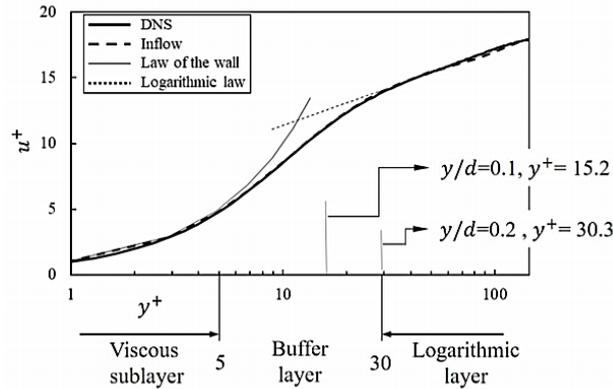
Fig. 8. Mean streamwise velocity profiles. y=d = 0:1;0:2 denote y⁺ = 15:2;30:3, respectively.

the range $y/d < 0.2$, and is shown to be similar to Case 02, although it is slightly larger in terms of shear stress. This is similar to the case having a short domain size of $x/d=12$ shown in Fig. 4(a), which implies that the domain needs to be at least longer than this size in the stream-wise direction to obtain fully developed turbulent statistics.

Case 04, which has a smaller length scale (i.e. $0.3L_z^*$) in the range $y/d < 0.2$, indicates that the shear stress has a local minimum turning point under this condition, and this means that the shear stress decreases and gradually recovers at a specific point around $x/d = 20$. However, the shear stress continues to increase, and finally becomes unstable at a point approximately 14 % higher than that of Case 01. For Case 05, in which the length scale is slightly smaller (i.e. $0.5L_z^*$) in the range $y/d < 0.2$, but larger (i.e. $1.5L_z^*$) for the rest of the range, the wall shear stress appears to be quite close to that of Case 01 in the inlet region; however, it appears scattered, wavy, and unstable downstream. Apart from Case 04, it does not tend to continue increasing continuously near the outlet, but it reaches a value that is 10 % higher than that in Case 01. In this study, we tried to adjust the size of the length scale in certain zones, such as $0.3L_z^*$ in L_z^* and L_z^* in $y/d > 0.1$, with the aim of understanding the effect of zone height on flow development. Interestingly, we foundthat the shear stress agrees fairly well with that in Case 01. This implies that depending on how the length scales are imposed in the zones, the wall shear stress would be adjusted in a target shape inside the domain.

Figure 7(b) shows the wall shear stress distribution for the cases with a larger inlet length scale (approximately two and/or three times) than that of Case 01 (i.e., L_z^*). Interestingly, Cases 07 and 08 (i.e. $2L_z^*$ and $3L_z^*$) show a faster recovery of the wall shear stress compared with Case 01. As shown in the figure, Case 08 has a higher length scale than Case 07, but the distance required to recover in the shear stress would be almost the same, whereas the

earlier drop in the shear stress close to the inlet in Case 08 was steeper than that in Case 07.

In case of the shear stress distribution of Case 01, Case 04, and Case 06 (see Fig. 7), these three cases have the same span-wise length scale of $1L_z^*$ at $y/d > 0.2$, but the conditions differ at $y/d < 0.2$. As shown in the figure, Cases 01 and 06 have very similar shear stress distributions, whereas Case 04 exhibits a markedly different tendency. The difference among these three cases is that the region with $0.3L_z^*$ exists at $y/d < 0.2$ for Case 04, and at $y/d < 0.1$ for Case 06. It can be observed that the change in the span-wise length scale in the range $0.1 < y/d < 0.2$ plays a significant influence on the development of the turbulent boundary layer.

Figure 8 shows the averaged turbulent boundary layer profile, and $y/d = 0.1$, 0.2 corresponds to $y^+ = 15.2, 30.3$, respectively, i.e. $y/d = 0.1$ is placed in the buffer layer and $y/d = 0.2$ in the logarithmic layer. With respect to the turbulence characteristics near the wall, some studies (Hinze 1975; Kline *et al.* 1967; Grass 1971) reported that the region close to the wall has a highly active turbulence movement, which is associated with the behaviour of low-speed streaks and horizontal shear stress in the span-wise direction. In addition, there is a breakup in the region $10 < y^+ < 30$, which is called 'bursting', contributing as much as 70 % of the turbulence. Kasagi *et al.* (1986) and Smith and Schwartz (1983) have identified counter-rotating stream-wise vortices in the region $14 \leq y^+ \leq 25$, which contains the most energetic vortices.

According to existing research, the $10 \leq y^+ \leq 30$ region contributes greatly to the generation of turbulence. As shown in Fig. 7, Cases 01 and 06 have the span-wise length scale of $1L_z^*$, which is a relatively large scale in $15 < y^+ < 30$, whereas Case 04 has $0.3L_z^*$, which means that it has a lower-length scale in this region, which is insufficient to generate

turbulence statistics. In addition, the lower-length scale reduces the energy production such that the minimum distance to recover the shear stress close to the wall is longer. It can be seen here that the change in the length scale in the region $y^+ < 15$ does not significantly impact the recovery of the shear stress. Therefore, the results of Case 01 and Case 06 are very similar. The change in the length scale in the approximate region of $15(0.1) < y^+(y/d) < 30(0.2)$ contributes significantly to the generation of turbulent energy near the wall surface.
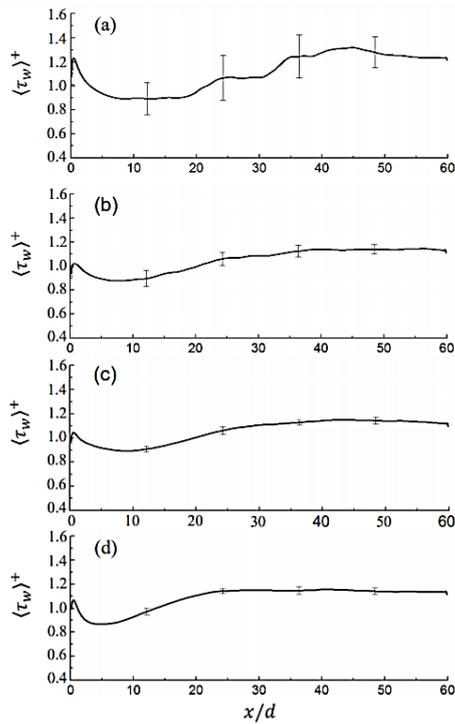
Fig. 9. Variation of dimensionless wall shear stress and deviation in the domain with changing length scales for (a) Case 05, (b) Case 06, (c) Case 01, (d) Case 08.

Figure 9 shows the stream-wise development of the wall shear stress $\langle \tau_w \rangle^+$ in the domain with the deviation, which indicates the magnitude of data variability as error bars. As the length scale near the wall becomes smaller (Case 05), the deviation becomes larger. Interestingly, as shown in the figure, Cases 01 and 06 are very close to each other, whereas the shear stress deviation of Case 06 is relatively large. In this case, the only difference is that Case 06 has a length scale of $0.3L_z^*$ in the region y/d < 0.1 (i.e., $y^+ < 15$). Therefore, if the span-wise length scale is small, the spatial correlation between two different points becomes lower such that this case requires a relatively long longitudinal length and time to fully develop in the domain. As the length scale increases, the wall shear stress tends to recover quickly. However, when the length scale is $2L_z^*$ or

more, the distance required for the full development of the boundary layer does not change significantly.

Figure 10(a) shows the change in the wall shear stress in the channel domain. In particular, Fig.10 (b), (c), (d), and (e) show the distribution of Reynolds stress profiles, $\langle u'u' \rangle^+, \langle v'v' \rangle^+, \langle w'w' \rangle^+$ at each longitudinal position of x/d. As depicted in the figure, Case 01 reveals that the downstream region has fully recovered the shear stress; however, Case 03 has a poor distribution in the domain. This implies that the size of the inlet length scale close to the wall, greatly influences the development of the shear stress. In addition, if the wall shear stress is fully recovered, the axial stresses $\langle u'u' \rangle^+, \langle v'v' \rangle^+, \langle w'w' \rangle^+$ remain constant in the whole domain.

Figure 11 compares the turbulent statistics in the boundary layer flow obtained downstream, at x/d = 50, from Case 01, Case 06, Case 07, and Case 08 with the data from the synthetic inflow generator in the inlet. As shown in the figure, the turbulent statistics at the inlet and downstream at x/d=50 clearly have a similar tendency. In Fig.11 (a), the axial longitudinal stress $\langle u'u' \rangle^+$ at x/d=50 appears similar near the wall surface compared to the inlet. However, when y/d is between 0.1 and 0.4, it is relatively lower than that of the inlet, and in the range 0.4 to 1.0, $\langle u'u' \rangle^+$ is relatively high. For x/d=50, all cases have a similar $\langle u'u' \rangle^+$ distribution. In Fig.11 (b), (c), and (d), the vertical $\langle v'v' \rangle^+$ and span-wise $\langle w'w' \rangle^+$ components of the axial and shear stresses, $\langle -u'v' \rangle^+$ at x/d = 50 were all slightly over-estimated compared to that at the inlet. When x/d = 50, it can be seen that the case having a larger inlet length scale has slightly lower stresses, except for $\langle u'u' \rangle^+$. This appears to be caused by the fact that the LES resolution is lower than that of DNS.

3.3 Effect of inlet length scale on the integral length scale in the domain

Figure 12 shows the longitudinal integral length scale of the stream-wise and vertical velocity (i.e. $L_x(u)$ and $L_x(w)$) at the inlet section (Fig.12 (a) and (c)) and at x/d = 50 (Fig.12 (b) and (d)). As shown in Fig.12 (a) and (c), in the cases close to the inlet, the magnitude of the integral length scale $L_x(u)/d$ close to the wall surface presents a large discrepancy when compared with existing DNS data. On the contrary, the length scales away from the wall (i.e. y/d > 0.5) are more similar. In particular, Case 09 (i.e. the case having the largest integral length scale at the inlet) has values very similar to the existing DNS data. The discrepancy between the length scales close to the wall may be due to the fact that the stream-wise length scale obtained from the actual DNS is for the fully developed profile; therefore, it is higher than that of the current study close to the wall and gradually decreases in the freestream. Interestingly, even though the length
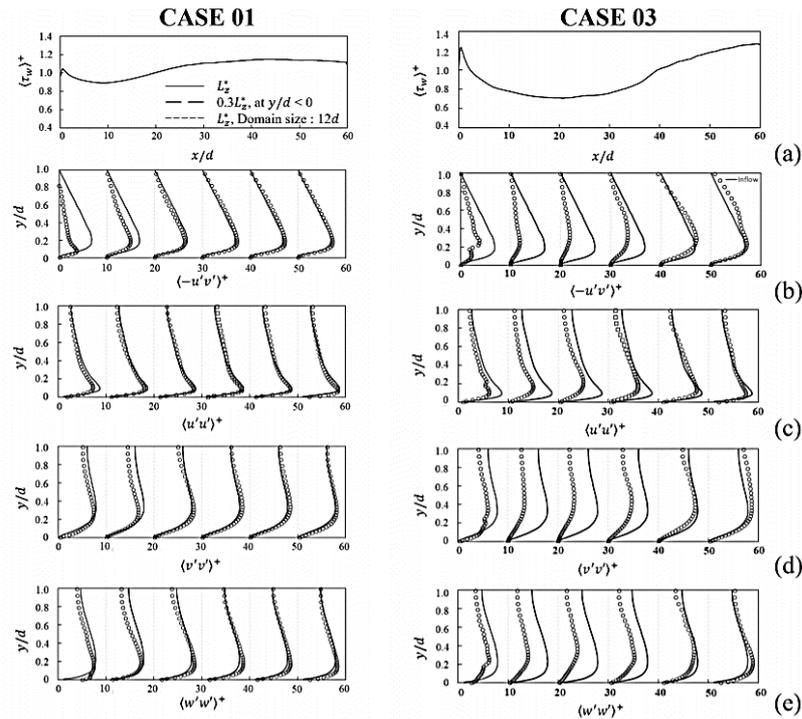
Fig. 10. Development of dimensionless wall shear stress and axial stresses. In the figure, at the left: Case 01, at the right: Case 03, solid line: DNS data, ○: simulation results.
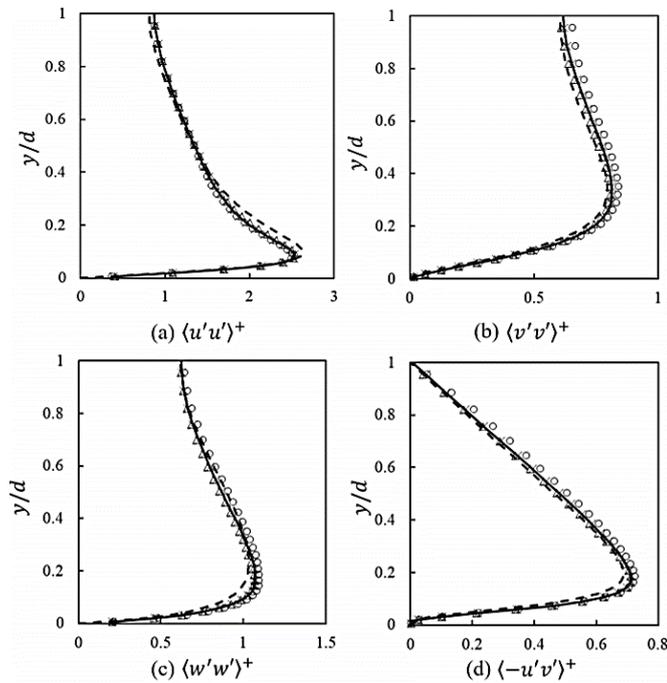

Fig. 11. **Mean and turbulent stress profiles at x/d = 50. In the figure, (a) $\langle u'u'\rangle^+$, (b) $\langle v'v'\rangle^+$,**

(c) $\langle w'w'\rangle^+$, (d) $\langle -u'v'\rangle^+$.

scale is different at the inlet (see Case 02 having no integral length scale at the inlet), the boundary layer develops, and the integral length scale profiles are almost equivalent downstream. This region is fully developed, except for regions that are proximal to the wall. As shown in Fig.12 (a) and (c), the longitudinal integral length scale of the vertical velocity (i.e. $L_x(w)$) at the inlet section would have the same
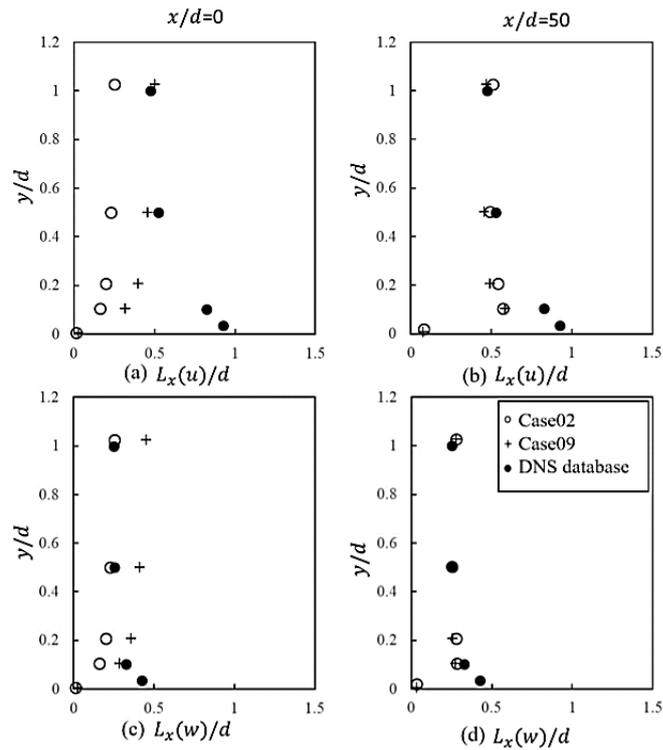
Fig. 12. Longitudinal integral length scale profiles at inlet section (a, c) and at *x/d* = 50 (b, d), *L_x(u)/d*: (a, b), *L_x(w)/d*: (a, b). In the figure, (a) denotes longitudinal integral length scales of streamwise velocity component at inlet section, (b) longitudinal integral length scales of streamwise velocity component at *x/d* = 50, (c) longitudinal integral length scales at the inlet section of spanwise velocity component, (d) longitudinal integral length scales of spanwise velocity component at *x/d* = 50, (° : Case01, + : Case09, • : DNS database).
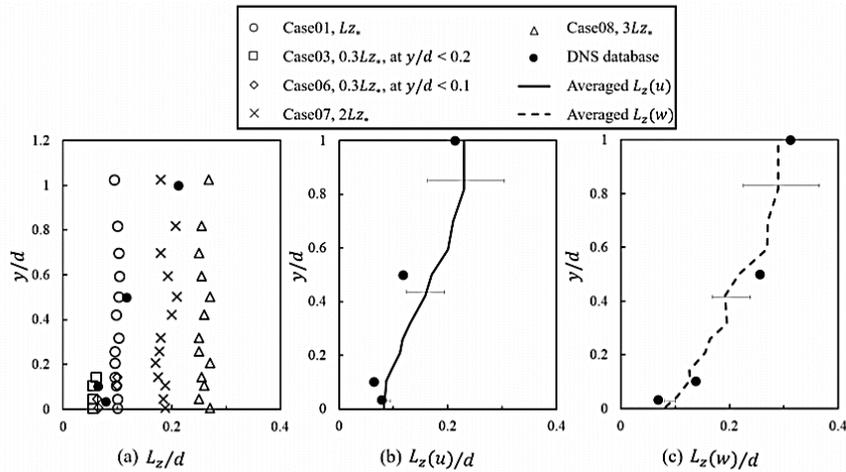

Fig. 13. Lateral integral length scale distribution at inlet and downstream sections. In the figure, (a) denotes all the lateral integral length scales at the inlet section (° : Case01, □: Case03, ◊ : Case06, × : Case07, △ : Case08, • : DNS database), and (b) the lateral integral length scale of streamwise velocity components at x/d = 50 (•: DNS database, _____: Averaged *L_z(u)*), and (c) the lateral integral length scale of spanwise velocity components at *x/d* = 50 (•: DNS database, : averaged *L_z(w)*).

tendency as the length scale of the stream-wise velocity (i.e. $L_x(u)$).

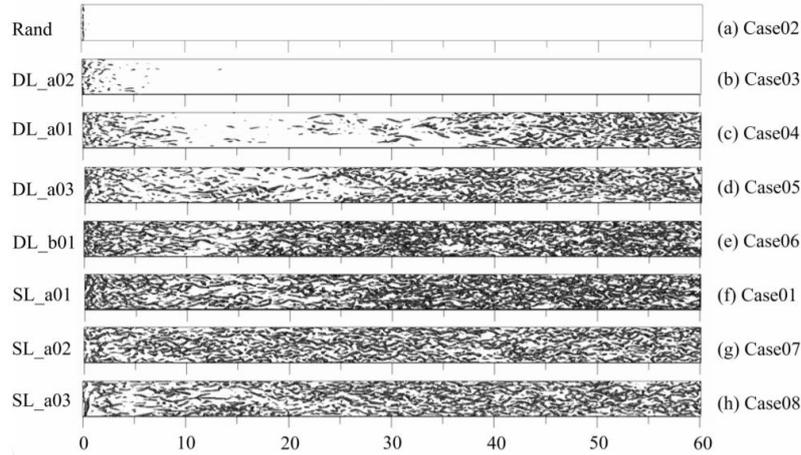Figure 13 shows the lateral integral length scale of the stream-wise and vertical velocity (i.e. $L_z(u)$ and

Fig. 14. Iso-surface of the Q-criterion at y=d < 0.25 and the value of Q > 1.

$L_z (w) $) at the inlet section (Fig.13 (a)) and at x/d = 50 (Fig.13 (b) and (c)). As mentioned earlier, regardless of the integral length scale at the inlet, the profiles observed downstream were similar, that is, they were fully developed.

3.4 Second invariant flow structure near the wall

A second invariant of the velocity gradient tensor can be used to visualise the flow structure near the wall. The related Q-criterion is defined as follows:

$$Q = \frac{1}{2}\left(\Omega_{ij}\Omega_{ij} - S_{ij}S_{ij}\right) \qquad (17)$$

where $\Omega_{ij} = \frac{1}{2}\left(\frac{\partial u_i}{\partial x_j} - \frac{\partial u_j}{\partial x_i}\right)$ and $S_{ij} = \frac{1}{2}\left(\frac{\partial u_i}{\partial x_j} + \frac{\partial u_j}{\partial x_i}\right)$.

Ω_{ij} denotes the rotation rate, and S_{ij} denotes the rate of the strain. From the equation, when Q is positive, it means that the intensity of the rotation rate is higher than the deformation rate.

Figure 14 shows the iso-surface of the Q-criterion in the range y/d<0.25 near the wall. The Q distribution shows a remarkably similar tendency to that of the wall shear stress $\langle \tau_w \rangle^+$ distribution in Fig.7. In fact, Case 03, as shown in Fig.7 tends to have a continuous reduction in the shear stress $\langle \tau_w \rangle^+$ from the inlet to x/d < 5, and this is also similar in the Q distribution. In Case 04, as shown in Fig.14(b), the Q structure was not observed in the region of 1 < x/d < 35. This means that when the shear stress is lower than 0.8, the vorticity strength is weak and therefore not enough to form the vortex. Thus, the vortex does not form. In addition, as the shear stress recovers, the vortex reforms when the shear stress is higher than 0.8.

In Fig. 14 (d), that is, in Case 05 and the cases having a length scale higher than 0.5 near the wall, the shear stress is higher than 0.8 in the entire region, and the vortex appears in the whole area. The vortex structure shows a slight discrepancy depending on the shear stress and the size of the length scale. Interestingly, in the region where the boundary layer is fully developed, the Q structures in all cases (Case 01, Case 07, Case 08) are similar.

Figure 15 shows the energy spectrum distribution at the inlet and for y/d = 50 compared to the existing DNS data. Figures 15(a) and (b) include the results of Case 01 (c) and (d) Case 09. As mentioned earlier, Case 09 has length scales that are two times larger in the stream-wise and span-wise directions compared with those of Case 01. In the figure, the symbol k is the wave number, which is defined as $2\pi f / U_m$. Figure 1522(a) and (c) show that the energy spectrum at the inlet has an appropriate level at the low wave number region; however, in the higher wave number region, it does not agree with the DNS data. In the figure, a dashed line has a slope of -5/3 in the spectrum. Regardless of the integral length scale at the inlet, the energy spectrum in the fully developed region agrees well with the DNS data.

4. CONCLUSION

To generate turbulent boundary layer flow in a numerical domain, a synthetic inflow generator having statistically well defined length scales was applied. It is based on spatial and temporal correlation functions, which have the form of an exponential function. To validate the turbulent boundary layer profiles that are obtained by using the synthetic inflow generator, the results obtained were precisely compared with existing data. From the results, it can be concluded that the turbulent boundary layer was successfully generated. In the mean velocity profile u^+, the boundary layer agrees well with the overall range of the domain, and the axial and shear stresses were in good agreement with the DNS data.

To observe the effect of the inflow length scales imposed at the inlet section on the development of a turbulent boundary layer, the length scales were varied with a focus on studying their effect. The results show that a larger length scale in the inlet
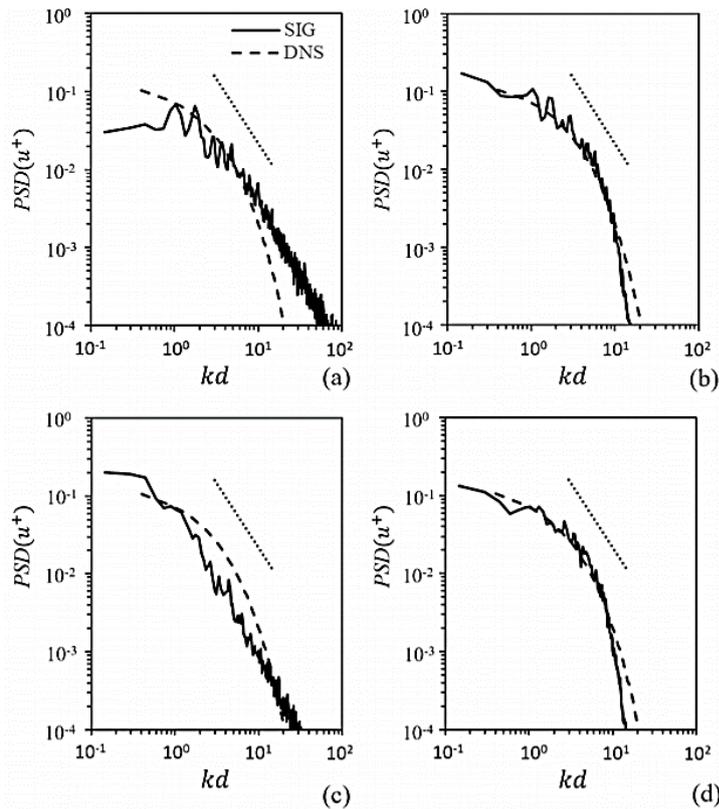
Fig. 15. Energy spectrum distribution at the inlet (a, c) and for *y/d* = 50 (b, d). In addition, (a) and (b) are the results from Case01, and (c) and (d) from Case09.

section had a faster rate of recovery in terms of the wall shear stress, which implies that larger length scales in the inlet section would be essential to the rapid development of the boundary layer, and thereby the realisation of a fully developed turbulent boundary layer.

In addition to the variation of the inlet length scale, the inlet plane was separated into two different zones with the aim of imposing two or three different length scales on each zone. The proximity of the wall was chosen to be approximately y/h = 0.1 and 0.2 so that the two ranges are first $0 < y^+ < 15$ (in the middle of the buffer layer zone) and $15 < y^+ < 150$, and secondly, $0 < y^+ < 30$ (in the buffer layer zone) and $30 < y^+ < 150$. Based on the results obtained, it can be seen that the length scale variation in the region $y^+ < 15$ does not significantly impact the recovery of the wall shear stress. However, the size of the length scale in the region of approximately $15 < y^+ < 30$ contributes significantly to the generation of turbulent energy near the wall surface.

ACKNOWLEDGEMENTS

REFERENCES

Deck, S., P. Weiss, M. Pamies and E. Garnier (2011). Zonal detached eddy simulation of a spatially developing flat plate turbulent boundary layer. *Computers & Fluids* 48(1), 1–15.

Druault, P., S. Lardeau, J. Bonnet, F. Coiffet, J. Delville, E. Lamballais, J. Largeau and L. Perret (2004). Generation of threedimensional turbulent inlet conditions for large-eddy simulation. *AIAA Journal* 42(3), 447– 456.

Grass, A. J. (1971). Structural features of turbulent flow over smooth and rough boundaries. *Journal of Fluid Mechanics* 50(2), 233–255.

Hanna, S., S. Tehranian, B. Carissimo and R. M. R. Lohner (2002). Comparisons of model simulations with observations of mean flow and

turbulence within simple obstacle arrays. *Atmospheric Environment* 36(32), 5067– 5079.

Hinze, J. (1975). *Turbulence*. NewYork: McGraw-Hill.

Iwamoto, K., Y. Suzuki and N. Kasagi (2002). Database of fully developed channel flow. department of mechanical engineering, the university of tokyo. *THTLAB Internal Report No. ILR-0201, DNS database(CH12 PG.WL7)(http:www.thtlab.t.utokyo.ac.jp* (1).

Jarrin, N., S. Benhamadouche, D. Laurence and R. Prosser (2006). A synthetic-eddy-method for generating inflow conditions for largeeddy simulations. *International Journal of Heat and Fluid Flow 27*, 585–593.

Johansson, P. and H. Andersson (2004). Theo. comp. fluid. dyn. *Fluid Dynamics Research* 18(5), 371–389.

Kasagi, N., M. Hirata and K. Nishino (1986). Streamwise pseudo-vortical structures and associated vorticity in the near-wall region of a wall-bounded turbulent shear flow. *Experiments in Fluids* 4(6), 309–318.

Keating, A., U. Piomelli, E. Balaras and H. Kaltenbach (2004). A priori and a posteriori tests of inflow conditions for large-eddy simulation. *Physics of Fluids* 16(12), 4696–4712.

Kim, J., P. Moin and R. Moser (1987). Turbulence statistics in fully developed channel flow at low reynolds number. *Journal of Fluid Mechanics 177*, 133–166.

Kim, Y.,I. Castro and Z. Xie(2013). Divergence-free turbulence inflow conditions for large-eddy simulations with incompressible flow solvers. *Computers & Fluids* 84, 56–68.

Kline, S., W. Reynolds, F. Schraub and P. Runstadler (1967). The structure of turbulent boundary-layers. *Journal of Fluid Mechanics* 30, 741–773.

Le, H. and P. Moin (2005). *Direct numerical simulation of turbulent flow over a backward-facing step*. Dept. of Mech. Engng., Standford Univ.: Report TF-58.

Lee, S., S. Lele and P. Moin (1992). Simulation of spatially evolving turbulence and the applicability of taylor hypothesis in compressible flow. *Physics of Fluids* 4(7), 1521–1530.

Lim, H., T. Thomas and I. Castro (2009). Flow around a cube in a turbulent boundary layer: LES and experiment. *Journal of Wind Engineering and Industrial Aerodynamics* 97(2), 96–109.

Lund, T., X. Wu and K. Squires (1998). Generation of turbulent inflow data for spatiallydeveloping boundary layer simulations. *Journal of Computational Physics* 140(2), 233–258.

Mare, L., M. Klein, W. Jones and J. Janicka (2006). Synthetic turbulence inflow conditions for large-eddy simulation. *Physics of Fluids* 18(2), 025107.

Moin, P. and J. Kim (1982). Numerical investigation of turbulent channel flow. *Journal of Fluid Mechanics* 118, 341–377.

Perret, L., J. Delville, R. Manceau and J.-P. Bonnet (2006). Generation of turbulent inflow conditions for large eddy simulation from stereoscopic piv measurements. *International Journal of Heat and Fluid Flow* 27(4), 576–584.

Smith, C. and S. Schwartz (1983). Smith, c., schwartz, s., 1983, observation of streamwise rotation in the near-wall region of a turbulent boundary layer. *Physics of Fluids* 26(3), 641–652.

Taylor, G. (1938). The spectrum of turbulence. proceedings of the royal society of london. *Series A. Mathematical, Physical and Engineering Sciences* 164(919), 476– 490.

Veloudis, I., Z. Yang, J. McGuirk, G. Page and A. Spencer (2007). Novel implementation and assessment of a digital filter based approach for the generation of LES inlet conditions. *Flow, Turbulence and Combustion* 79(1), 1–24.

Xie, Z. and I. Castro (2008). Efficient generation of inflow conditions for large eddy simulation of street-scale flows. *Flow, Turbulence and Combustion* 81(3), 449–470.